BULLETIN OF THE POLISH ACADEMY OF SCIENCES
TECHNICAL SCIENCES, Vol. 69(3), 2021, Article number: e137065
DOI: 10.24425/bpasts.2021.137065

NFTSM control of direct yaw moment for autonomous electric vehicles with consideration of tire nonlinear mechanical properties

Xiaoqiang SUN[1,2]*, Yujun WANG[1], Yingfeng CAI[1], Pak Kin WONG[3], and Long CHEN[2]

[1] Automotive Engineering Research Institute, Jiangsu University, Zhenjiang Jiangsu, China
[2] State Key Laboratory of Automotive Safety and Energy, Tsinghua University, Beijing, China
[3] Department of Electromechanical Engineering, University of Macau, Taipa, Macau

Abstract. To improve the curve driving stability and safety under critical maneuvers for four-wheel independent drive autonomous electric vehicles, a three-stage direct yaw moment control (DYC) strategy design procedure is proposed in this work. The first stage includes modeling of the tire nonlinear mechanical properties, i.e. the coupling relationship between the tire longitudinal force and the tire lateral force, which is crucial for the DYC strategy design, in the STI (Systems Technologies Inc.) form based on experimental data. On this basis, a 7-DOF vehicle dynamics model is established and the direct yaw moment calculation problem of the four-wheel independent drive autonomous electric vehicle is solved through the nonsingular fast terminal sliding mode (NFTSM) control method. Thus optimal direct yaw moment can be obtained. To achieve this direct yaw moment, an optimal allocation problem of the tire forces is further solved by using the trust-region interior-point method, which can effectively guarantee the solving efficiency of a complex optimization problem such as the tire driving and braking forces allocation of four wheels in this work. Finally, effectiveness of the DYC strategy proposed for autonomous electric vehicles is verified through the CarSim-Simulink co-simulation results.

Key words: autonomous electric vehicles; direct yaw moment control (DYC); tire nonlinear mechanical properties; nonsingular fast terminal sliding mode (NFTSM); trust-region interior-point method.

1. Introduction

With the problems of energy, pollution and traffic safety in the world becoming increasingly serious, traditional vehicles should speed up their transformation in the electric and intelligent directions [1–3]. In recent years, the field of autonomous electric vehicles has attracted more and more attention. The four-wheel independent drive autonomous electric vehicle is just one of the many iconic products in line with this trend [4]. It not only has the advantages of short drive chain, high transmission efficiency and compact structure, but also it is convenient for vehicle stability control design under autonomous curve driving conditions because of the independently controllable driving and braking forces of each wheel [5, 6].

In fact, several studies have been conducted to improve the curve driving stability and safety under critical maneuvers for the autonomous electric vehicles and they all entail calculating an optimal direct yaw moment [7–12]. However, although these studies have made great efforts in the DYC algorithm design, the model accuracy of the controlled object is always ignored. In fact, the DYC system is only activated under those driving conditions in which the vehicle system presents high nonlinearity, especially the tires [13]. Thus, the tire nonlinear mechanical properties, especially the coupling relationship between the tire longitudinal force and tire lateral force, focused on in this work, must be considered carefully during the design procedure of the DYC strategy. As it constitutes one of the most important components of vehicle system dynamics, great attention has certainly been paid to the modeling of tire mechanical properties. However, many tire models cannot reflect the tire forces coupling relationship effectively. Therefore, previous studies based on a simple tire model cannot achieve satisfactory DYC performance in practical applications. To solve this problem, a tire nonlinear mechanical properties model in the STI form, which is proposed by an American company named "Systems Technologies Inc." [14, 15], is considered to be used in this work. The STI tire model can not only accurately reflect tire nonlinear properties, but also focus on describing the coupling relationship between the tire longitudinal force and tire lateral force, thus it is very suitable for DYC strategy design in which the calculation of the optimal direct yaw moment must consider the tire forces coupling relationship.

Based on an accurate model of the system, the effectiveness of the DYC strategy can then be guaranteed. Recently, several methodologies have been adopted in DYC strategy design, such as the fractional order PID control [16], nonlinear model predictive control [17], non-smooth control [18] and slide mode control (SMC) [19]. Among them, the SMC methods have shown high overall control performance due to their strong robustness against uncertainties and disturbances. However, traditional SMC methods still have drawbacks, thus much attention has been paid to improve them [20–22]. At this stage, one of the effective improvement methods is the nonsingular fast

*e-mail: sxq@ujs.edu.cn

Manuscript submitted 2020-08-17, revised 2021-03-09, initially accepted for publication 2021-03-28, published in June 2021

terminal sliding mode (NFTSM) control method. This method can achieve fast convergence and chattering elimination simultaneously [23, 24], thus it can be applied in this work to calculate the optimal direct yaw moment. On this basis, it is obvious that an optimal allocation problem of the tire forces should then be solved. Although several algorithms have achieved effective allocation of the tire forces [25–27], the calculation time is still too long for the complex optimization problem such as the tire forces allocation in this work, which cannot be accepted by the actual DYC strategy design. Thus, a novel numerical method for solving nonlinear programming problems, i.e. the trust-region interior-point method [28–30], is adopted in this work to achieve the real-time solution of the optimal allocation problem of the four wheel forces.

According to the above descriptions, modeling of tire nonlinear mechanical properties in the STI form, the NFTSM control algorithm used for calculating the optimal direct yaw moment and the optimal allocation of the tire forces of four wheels based on the trust-region interior-point method are the three unique features of this research. These three points are essential for moving forward the scientific and industrial knowledge on DYC strategy design. Although the aforementioned methods are not innovatory for this research from a separate perspective, it is of great significance to combine them to achieve DYC strategy design for autonomous electric vehicles. By conducting this work, the tire forces coupling relationship is considered more comprehensively, the calculated direct yaw moment becomes more reasonable and the solution of the optimal allocation problem of the tire forces is quicker. Thus the DYC system is rendered more suitable for real-world vehicle implementations.

The organization of this paper is as follows: modeling of the tire nonlinear mechanical properties in the STI form and establishment of a 7-DOF vehicle dynamics model are reported on in Section 2. Calculation of the optimal direct yaw moment based on the NFTSM control algorithm is given in Section 3. The optimal allocation of the tire forces by using the trust-region interior-point method is reported in Section 4. The CarSim-Simulink co-simulation study used to verify the effectiveness of the DYC strategy is shown in Section 5. Finally, the conclusions are provided in Section 6.

2. System description and modeling

2.1. Tire nonlinear mechanical properties modeling. In this work, to reduce computational complexity and facilitate the real-time application in DYC system, the STI tire model is firstly simplified on the premise of ensuring model accuracy and preserving the whole structure of the tire model. Meanwhile, to obtain the most accurate tire model parameters, tire tests are conducted, thus the STI tire model parameters can be fitted accurately based on the experimental data, which is highly consistent with the tire actual mechanical characteristics.

2.1.1. STI tire model description. To model the tire mechanical properties in the STI form, the composite slip coefficient σ must be defined firstly as [31]:

$$\sigma = \frac{\pi a_p^2 \sqrt{k_\alpha^2 \tan^2\alpha + k_s^2 (s/(1-s))^2}}{8\mu F_z}, \tag{1}$$

where a_p is the tire contact patch length, k_α is the tire lateral stiffness, k_s is the tire longitudinal stiffness, α is the tire slip angle, s is the tire slip ratio, μ is the road adhesion coefficient and F_z is the tire vertical load. According to the expression of the composite slip coefficient, it can be seen that many factors are considered carefully, thus the STI tire model can precisely describe the tire mechanical characteristics under composite conditions on this basis.

In Eq. (1), the length of the tire contact patch can be further defined as [15]:

$$a_p = \frac{0.0768\sqrt{F_z \cdot F_{zt}}}{T_w(T_p+5)}, \tag{2}$$

where F_{zt} is the tire design load, T_w is the tire width and T_p is the tire pressure. Tire lateral stiffness k_α and tire longitudinal stiffness k_s in Eq. (1) can be measured by means of experimental tests. On this basis, to further consider the saturation effect of the tire longitudinal stiffness, modified tire longitudinal stiffness k_{sm} is defined as:

$$k_{sm} = k_s + (k_\alpha - k_s)\sqrt{\sin^2\alpha + \cos^2\alpha}. \tag{3}$$

Based on the defined composite slip coefficient σ, a tire force saturation function is further defined as:

$$f(\sigma) = \frac{C_1\sigma^3 + C_2\sigma^2 + (4/\pi)\sigma}{C_1\sigma^3 + C_3\sigma^2 + C_4\sigma + 1}, \tag{4}$$

where C_1, C_2, C_3 and C_4 are the fixed coefficients, which can be obtained by fitting the experimental data. Function $f(\sigma)$ is consistent with the mechanical properties of the tire force friction circle, thus it can reflect the tire force saturation characteristics effectively. Then, on the basis of the above equations, the standardized expressions of the tire longitudinal force and tire lateral force in the STI form can be described, respectively, as:

$$\begin{cases} F_x = \dfrac{f(\sigma)k_{sm}s}{\sqrt{k_\alpha^2\tan^2\alpha + k_{sm}^2 s^2}}\mu F_z, \\ F_y = \dfrac{f(\sigma)k_\alpha\tan\alpha}{\sqrt{k_\alpha^2\tan^2\alpha + k_{sm}^2 s^2}}\mu F_z + Y_\gamma\gamma, \end{cases} \tag{5}$$

where F_x is the tire longitudinal force, F_y is the tire lateral force, γ is the tire camber angle and Y_γ is the tire camber coefficient. As can be seen in Eq. (5), the coupling relationship between the tire longitudinal force and tire lateral force is reflected in an exact manner.

2.1.2. Tire mechanical properties tests. To obtain the experimental data which can accurately reflect the tire nonlinear mechanical properties, tire mechanical properties tests are conducted. During the tire test process, three different tire vertical loads, reasonable tire slip range ($-1\sim0.5$), tire sideslip angle

range (−15°∼15°) and two road longitudinal adhesion coefficients are achieved. The tire camber angle is assumed to be zero, thus the influence of the camber angle on the tire lateral force shown in Eq. (5) is not considered in this work. The tire slip range is set as $[-1, 0.5]$, which means that the tire can be completely locked when braking, while for driving on slippery roads, the maximum tire slip is set to 0.5. The specific parameter settings of the tire mechanical properties tests are provided in Table 1.

Table 1
List of parameter settings

Parameter	Setting
Tire pressure (kPa)	880
Tire width (m)	0.114
Tire design load (kN)	12
Vertical load (N)	8060, 9480, 11770
Tire slip angle (°)	−15∼15
Longitudinal slip ratio	−1∼0.5
Adhesion coefficient	0.34, 0.77

2.1.3. Tire model parameters fitting. Based on the experimental data, the parameters of the STI tire model can then be fitted. According to the expressions of the tire forces, it is obvious that the parameters to be fitted are the four fixed coefficients C_1, C_2, C_3 and C_4 in Eq. (4). Consider the case of the tire bench test under the low road adhesion coefficient: the STI tire model parameters fitting process is shown in Fig. 1.

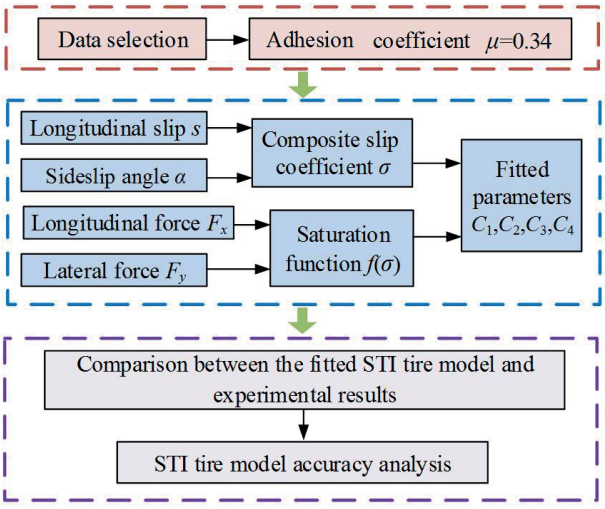

Fig. 1. STI tire model parameter fitting process

Before achieving the fitting of the four coefficients C_1, C_2, C_3 and C_4, tire lateral stiffness k_α and tire longitudinal stiffness k_s should be measured based on the experimental test results firstly. On this basis, the value of the composite slip coefficient σ can then be calculated for different tire vertical loads, tire slip angles and tire longitudinal slip ratios. Meanwhile, the tire force saturation function can also be determined based on the experimental results and Eq. (5). Therefore, by combining the value of the composite slip coefficient and the value of the tire force saturation function, the fixed coefficients C_1, C_2, C_3 and C_4 can then be determined by using the curve fitting function. Finally, the values of the four fixed coefficients C_1, C_2, C_3 and C_4 are determined as 6.5, 4.54, 4.6 and 0.25, respectively.

Based on the fitted tire force saturation function, the tire force comparisons between the experimental results and the simulation results of the STI tire model are further shown in Fig. 2 and Fig. 3, where the solid lines represent the fitting data and the lines with data points represent the experimental data. As can be seen from these two figures, the simulation results of the STI tire model are in good agreement with the experimental results, which indicates that the derived STI tire model can accurately describe the tire nonlinear mechanical properties and the coupling relationship between the tire longitudinal force and tire lateral force.

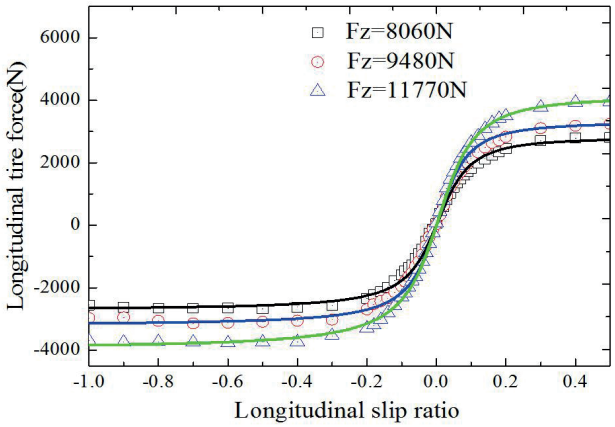

Fig. 2. Tire longitudinal force comparison

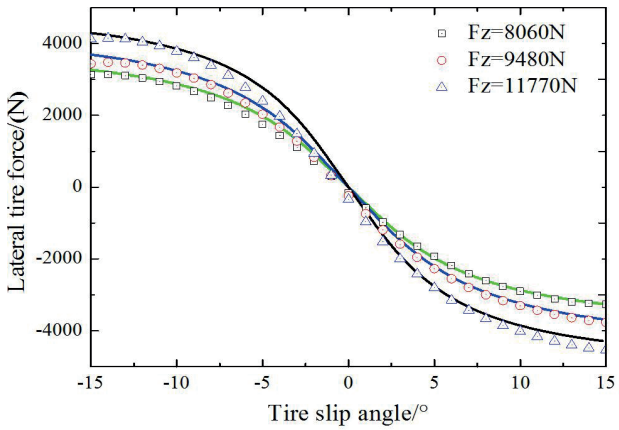

Fig. 3. Tire lateral force comparison

2.2. Vehicle dynamics modeling. In this section, a 7-DOF vehicle dynamics model is established for the four-wheel independent drive electric vehicle based on previous literature [32–34].

The vehicle 7-DOF dynamic model includes the longitudinal motion, lateral motion, yaw motion and rotational dynamics of the four wheels. Based on Newton's theorem, the related dynamic equations are given by [35–37]:

$$\begin{cases} m(\dot{v}_x - r\cdot v_y) = (F_{xfl}+F_{xfr})\cos\delta - (F_{yfl}+F_{yfr})\sin\delta \\ \qquad\qquad + F_{xrl}+F_{xrr}, \\ m(\dot{v}_y + r\cdot v_x) = (F_{xfl}+F_{xfr})\sin\delta + (F_{yfl}+F_{yfr})\cos\delta \\ \qquad\qquad + F_{yrl}+F_{yrr}, \\ I_z\cdot\dot{r} = \left[(F_{xfl}+F_{xfr})\sin\delta + (F_{yfl}+F_{yfr})\cos\delta\right] a \\ \qquad + \left[(F_{xfr}-F_{xfl})\cos\delta + (F_{yfl}-F_{yfr})\sin\delta\right]\dfrac{t_{w1}}{2} \\ \qquad + (F_{xrr}-F_{xrl})\dfrac{t_{w2}}{2} - (F_{yrl}-F_{yrr})b, \end{cases} \tag{6}$$

where F_{xij} and F_{yij} denote the tire longitudinal and lateral forces, respectively, the first subscript $i = f$ or r represent front and rear axles, respectively, and the second $j = l$ or r denote left and right wheels. m is the vehicle mass, v_x and v_y are the longitudinal and lateral velocities of the vehicle, δ is the front wheel steering angle, a is the distance from the center of the vehicle to the front axle, b is the distance from the center to the rear axle, t_{w1} and t_{w2} are the wheel bases of the front and rear axles and r is the vehicle yaw rate. It is noted that the tire longitudinal and lateral forces in Eq. (6) are calculated by the STI tire model which has been established in the previous section.

The dynamic equations which describe the rotation motion of the four wheels are given by:

$$J\cdot\dot{\omega}_k = T - F_{xij}\cdot R, \tag{7}$$

where J is the moment of inertia of the wheel, ω_k $(k = 1,2,3,4)$ represent the angular velocities of the four wheels, R is the wheel radius and T_k $(k = 1,2,3,4)$ represent the driving or braking torques acting on the four wheels.

Considering that the vehicle load will transfer during the vehicle curve driving process, thus the tire dynamic vertical load can be calculated by combining the static tire vertical load and the load transfer effect caused by longitudinal and lateral acceleration. Thus, the related equations of the tire vertical load are expressed as [38, 39]:

$$\begin{cases} F_{zfl} = mg\dfrac{b}{2l} - ma_x\dfrac{h_g}{2l} - ma_y\dfrac{h_g}{t_{w1}}\cdot\dfrac{b}{l}, \\ F_{zfr} = mg\dfrac{b}{2l} - ma_x\dfrac{h_g}{2l} + ma_y\dfrac{h_g}{t_{w1}}\cdot\dfrac{b}{l}, \\ F_{zrl} = mg\dfrac{a}{2l} + ma_x\dfrac{h_g}{2l} - ma_y\dfrac{h_g}{t_{w1}}\cdot\dfrac{a}{l}, \\ F_{zrr} = mg\dfrac{a}{2l} + ma_x\dfrac{h_g}{2l} + ma_y\dfrac{h_g}{t_{w1}}\cdot\dfrac{a}{l}, \end{cases} \tag{8}$$

where h_g is the height of the vehicle center, l is the length of the electric vehicle, and the lateral and longitudinal accelerations of the vehicle are respectively expressed as:

$$\begin{cases} a_x = \dot{v}_x - r\cdot v_y \\ a_y = \dot{v}_y + r\cdot v_x \end{cases}. \tag{9}$$

In addition, the calculation of the tire slip angle of each wheel can be given as follows:

$$\begin{cases} \alpha_{fl} = \delta - \arctan\left(\dfrac{v_y + ar}{v_x - t_{w1}r/2}\right) \\ \alpha_{rl} = \delta - \arctan\left(\dfrac{v_y + ar}{v_x + t_{w1}r/2}\right) \\ \alpha_{rl} = -\arctan\left(\dfrac{v_y - br}{v_x - t_{w2}r/2}\right) \\ \alpha_{rl} = -\arctan\left(\dfrac{v_y - br}{v_x + t_{w2}r/2}\right) \end{cases}. \tag{10}$$

Since the vehicle driving states have been calculated, the wheel center speed of each wheel can then be obtained as follows [40]:

$$\begin{cases} v_{t\_fl} = \left(v_x - \dfrac{t_{w1}}{2}r\right)\cos\delta + (v_y + ar)\sin\delta \\ v_{t\_fr} = \left(v_x + \dfrac{t_{w1}}{2}r\right)\cos\delta + (v_y + ar)\sin\delta \\ v_{t\_rl} = v_x - \dfrac{t_{w2}}{2}r, \quad v_{t\_rr} = v_x + \dfrac{t_{w2}}{2}r \end{cases}. \tag{11}$$

By combining angular velocity and the wheel center speed of the four wheels, the tire longitudinal slip ratio can then be calculated by:

$$\begin{cases} s_{fl} = \dfrac{\omega_{fl}R - v_{t\_fl}}{v_{t\_fl}}, \quad s_{fr} = \dfrac{\omega_{fr}R - v_{t\_fr}}{v_{t\_fr}} \\ s_{rl} = \dfrac{\omega_{rl}R - v_{t\_rl}}{v_{t\_rl}}, \quad s_{rr} = \dfrac{\omega_{rr}R - v_{t\_rr}}{v_{t\_rr}} \end{cases}. \tag{12}$$

As can be seen from the above equations, the tire vertical load, the tire slip angle and the tire longitudinal slip ratio can be calculated by the vehicle dynamics model in real time, thus on this basis, the tire longitudinal and lateral forces can be calculated through the established tire model in the STI form, which lays an important foundation for the following DYC system design.

3. DYC strategy design

By establishing the 7-DOF vehicle dynamics model whose tire forces are calculated by the STI tire model with fitting parameters, the vehicle DYC system design can then be achieved in this section through the NFTSM control algorithm.

3.1. Control system structure. The control objective of the DYC system for the four-wheel independent drive autonomous electric vehicle is to improve the curve driving stability and safety under critical maneuvers by enabling the vehicle driving states to track the target values calculated by the reference model. As mentioned before, the DYC system is only activated under those driving conditions in which the tire-road friction

force cannot meet the requirements of both the tire longitudinal force and tire lateral force [41], thus the first task of the DYC system design is to calculate an optimal direct yaw moment by considering the tire forces coupling relationship carefully through the STI tire model. On this basis, a real-time allocation algorithm should be further adopted to distribute the driving and braking forces of the four wheels, thus the optimal direct yaw moment can be achieved effectively. Finally, to verify the effectiveness of the designed DYC strategy, the CarSim vehicle model, which can accurately reflect the nonlinear dynamic characteristics of vehicles, is adopted to conduct the co-simulation work with Simulink.

3.2. Reference model. Just like in other research [42], the 2-DOF vehicle model, i.e. the linear bicycle model, is adopted in this work as the reference model to compute the reference control objectives. The concrete expressions of the 2-DOF vehicle model can be written as:

$$\begin{cases} \dot{\beta} = \dfrac{k_f + k_r}{m v_x}\beta + \left(\dfrac{a k_f - b k_r}{m v_x^2} - 1\right) r - \dfrac{k_f}{m v_x}\delta \\ \dot{r} = \dfrac{a k_f - b k_r}{I_z}\beta + \dfrac{a^2 k_f + b^2 k_r}{I_z v_x} r - \dfrac{a k_f}{I_z}\delta \end{cases}, \tag{13}$$

where β is the vehicle slip angle while k_f and k_r denote the cornering stiffness of the front tire and the rear tire.

On this basis, the reference vehicle yaw rate and slip angle can be obtained as follows:

$$r_d = \min\left\{\left|\frac{v_x/L}{1+Kv_x^2}\delta\right|, \left|\frac{\mu g}{v_x}\right|\right\}\cdot \mathrm{sgn}(\delta), \tag{14}$$

$$\beta_d = \min\left\{\left|\frac{b/L + m a v_x^2/(k_r L^2)}{1+Kv_x^2}\delta\right|, \left|\mu g\left(\frac{b}{v_x^2} + \frac{ma}{k_r L}\right)\right|\right\}\cdot \mathrm{sgn}(\delta), \tag{15}$$

where r_d is the reference yaw rate, β_d is the reference vehicle slip angle and K is the stability factor, which is expressed as:

$$K = \frac{m}{L^2}\left(\frac{a}{k_r^2} - \frac{b}{k_f^2}\right). \tag{16}$$

3.3. Calculation of the optimal direct yaw moment. To ensure that the position and attitude of the four-wheel independent drive autonomous electric vehicle can be operated in a reasonable range when tracking curve paths under critical maneuvers, an optimal direct yaw moment is calculated in this section. Firstly, according to the specific definition of the NFTSM control algorithm, the following first-order terminal sliding mode variable is defined as [43–45]:

$$s = e + \frac{1}{\alpha_1} e^{g_1/h_1} + \frac{1}{\beta_1}\dot{e}^{p_1/q_1}, \tag{17}$$

where α_1, $\beta_1 \in R^+$, p_1, q_1, g_1 and $h_1 \in N^+$ are positive odd integers which satisfy $1 < p_1/q_1 < 2$, $g_1/h_1 > p_1/q_1$.

In Eq. (17), e represents the system tracking error, which is always expressed as:

$$\begin{cases} e = c_1(\beta - \beta_d) + (1-c_1)(\varphi - \varphi_d) \\ \dot{e} = c_1\left(\dot{\beta} - \dot{\beta}_d\right) + (1-c_1)(r - r_d) \\ \ddot{e} = c_1\left(\ddot{\beta} - \ddot{\beta}_d\right) + (1-c_1)(\dot{r} - \dot{r}_d) \end{cases}, \tag{18}$$

where c_1 is the weight coefficient used to determine the control specific proportion of the vehicle slip angle and the yaw rate, and φ is the vehicle yaw angle. On this basis, the time derivative of the sliding mode variable defined by Eq. (17) can be obtained by:

$$\begin{aligned} \dot{s} &= \dot{e} + \frac{g_1}{\alpha_1 h_1} e^{g_1/h_1 - 1}\dot{e} + \frac{p_1}{\beta_1 q_1}\dot{e}^{p_1/q_1 - 1}\ddot{e} \\ &= \dot{e} + \frac{g_1}{\alpha_1 h_1} e^{g_1/h_1 - 1}\dot{e} \\ &\quad + \frac{p_1}{\beta_1 q_1}\dot{e}^{p_1/q_1 - 1}\left[c_1\left(\ddot{\beta} - \ddot{\beta}_d\right) + (1-c_1)(\dot{r} - \dot{r}_d)\right], \end{aligned} \tag{19}$$

To reduce the chattering phenomenon and ensure control input continuity of the system, a terminal attractor with the negative exponential factor is further adopted in this work to design the sliding surface reaching law [46]:

$$\dot{s} = (-k_1 s - r_1)\, s^{m_1/q_1 - 1}, \tag{20}$$

where k_1, $r_1 \in R^+$, m_1 and $n_1 \in N^+$ are positive odd integers which satisfy $0 < m_1/n_1 < 2$. Combining the above two equations, the NFTSM control law, used for calculating the optimal direct yaw moment, is derived as:

$$\begin{aligned} &\dot{e} + \frac{g_1}{\alpha_1 h_1}\cdot e^{g_1/h_1 - 1}\dot{e} \\ &\quad + \frac{p_1}{\beta_1 q_1}\dot{e}^{p_1/q_1 - 1}\left\{c_1\left(\ddot{\beta} - \ddot{\beta}_d\right) + (1-c_1)\left[\dot{r} - \dot{r}_d\right]\right\} \\ &\qquad = \left(-k_1 s - r_1 s^{m_1/n_1}\right)\dot{e}^{p_1/q_1 - 1}. \end{aligned} \tag{21}$$

We then further transform the expression of the vehicle yaw motion in Eq. (6) as:

$$\begin{aligned} \dot{r} = \frac{1}{I_z}\Big[&\frac{t_{w1}}{2}(F_{yfl} - F_{yfr})\sin\delta + a(F_{yfl} + F_{yfr})\cos\delta \\ &- b\left(F_{yrl} + F_{yrr}\right) + M_z\Big], \end{aligned} \tag{22}$$

where M_z is the direct yaw moment, which is expressed as:

$$\begin{aligned} M_z = &a(F_{xfl} + F_{xfr})\sin\delta - \frac{t_{w1}}{2}(F_{xfl} - F_{xfr})\cos\delta \\ &- \frac{t_{w2}}{2}(F_{xrl} - F_{xrr}). \end{aligned} \tag{23}$$

Combining Eq. (21), (22) and (23), the control law can be further expressed as:

$$\dot{e}+\frac{g_1}{\alpha_1 h_1}\cdot e^{g_1/h_1-1}\dot{e} + \frac{p_1}{\beta_1 q_1}\dot{e}^{p_1/q_1-1}\left\{c_1(\ddot{\beta}-\ddot{\beta}_d)+(1-c_1)\left[\frac{1}{I_z}(P+M_z)-\dot{r}_d\right]\right\} = (-k_1 s - r_1 s^{m_1/n_1})\dot{e}^{p_1/q_1-1}, \quad (24)$$

where:

$$P=\frac{t_{w1}}{2}\left(F_{yfl}-F_{yfr}\right)\sin\delta + a\left(F_{yfl}+F_{yfr}\right)\cos\delta - b\left(F_{yrl}-F_{yrr}\right). \quad (25)$$

Therefore, the calculation of the vehicle direct yaw moment based on the NFTSM control algorithm can be derived as follows:

$$M_z = I_z\cdot\dot{r}_d - P - \frac{I_z}{1-c_1}\left\{c_1\left(\ddot{\beta}-\ddot{\beta}_d\right) + \frac{\beta_1 q_1}{p_1}\left[\begin{array}{l}\left(1+\frac{g_1}{\alpha_1 h_1}\cdot e^{g_1/h_1-1}\right)\dot{e}^{2-p_1/q_1}\\ +\left(k_1 s + r_1 s^{m_1/n_1}\right)\end{array}\right]\right\}. \quad (26)$$

Based on Lyapunov theory, the proof process of the control system stability can be analyzed as follows [47]:

Define the control system Lyapunov function as $V=0.5s^2$, and the time derivative of V can then be obtained as:

$$\dot{V}=s\dot{s}=s\left\{\begin{array}{l}\dot{e}+\frac{g_1}{\alpha_1 h_1}e^{g_1/h_1-1}\dot{e}\\ +\frac{p_1}{\beta_1 q_1}\dot{e}^{p_1/q_1-1}\left[\begin{array}{l}c_1\left(\ddot{\beta}-\ddot{\beta}_d\right)\\ +(1-c_1)\left(\dot{r}-\dot{r}_d\right)\end{array}\right]\end{array}\right\}. \quad (27)$$

When substituting the nonsingular fast terminal sliding control law as Eq. (19) into Eq. (26), it can be concluded that:

$$\dot{V}=s\dot{s}=s\left(-k_1 s - r_1 s^{m_1/n_1}\right)\dot{e}^{p_1/q_1-1}. \quad (28)$$

Since p_1 and q_1 are positive odd integers with $1<p_1/q_1<2$, thus the following relation exist:

$$\dot{e}^{p_1/q_1-1}>0 \quad \text{if } \dot{e}\neq 0. \quad (29)$$

Thus, on this basis, the system Lyapunov function satisfies the following:

$$\dot{V}=s\dot{s}=\left(-k_1 s^2 - r_1 s^{m_1/n_1+1}\right)\dot{e}^{p_1/q_1-1}<0 \quad \text{if } \dot{e}\neq 0. \quad (30)$$

When $\dot{e}=0$, the following inequality is satisfied:

$$\ddot{e}=-\frac{\beta_1 q_1}{p_1}\left(k_1 e + r_1 e^{m_1/n_1}\right)<0. \quad (31)$$

Thus, the time derivative of the control system Lyapunov function also satisfies the following:

$$\dot{V}=s\dot{s} = (p_1/q_1-1)\left(-k_1 s^2 - r_1 s^{m_1/n_1+1}\right)\dot{e}^{p_1/q_1-2}\ddot{e}<0. \quad (32)$$

According to the above analysis process, the system state can asymptotically converge to zero along the sliding surface $s=0$ in finite time, which proves the stability of the proposed NFTSM control system.

4. Optimal allocation of tire forces

In this section, we discuss in detail how the obtained optimal direct yaw moment can be further achieved by distributing the forces of the four wheels.

4.1. Description of the dynamic allocation problem. Since the research objective in this work is a four-wheel independent drive autonomous electric vehicle, thus the optimal direct yaw moment will be achieved through the actuators, i.e. the four electric motors, of the electric vehicle [48–50]. Meanwhile, note that since the DYC system is only activated under those driving conditions in which the tire-road friction force cannot meet the requirements of both the tire longitudinal force and tire lateral force, thus the tire forces coupling relationship should also be satisfied for a single wheel in the dynamic allocation procedure. However, this treatment will make the dynamic allocation problem more difficult when considering the tire force constraints in longitudinal direction and lateral direction. Therefore, how to conduct the dynamic allocation of all the tire forces to achieve the desired yaw moment is actually a challenging research task [51]. Considering the real-time and effectiveness requirements of the solution of the dynamic allocation problem, the trust-region interior-point method, which combines the trust-region method with the traditional interior-point method, is adopted in this work to solve the optimal allocation problem of the tire forces.

Firstly, the allocation objective function of the tire forces can be expressed as:

$$f=A_{ij}\frac{F_{xij}^2+F_{yij}^2}{\left(\mu F_{zij}\right)^2}, \quad (33)$$

where A_{ij} is the weight coefficient for each tire and μ is the road adhesion coefficient. Define the target longitudinal force and lateral force of the four tires as vector x:

$$x=\left[\begin{array}{cccccccc}F_{xfl} & F_{xfr} & F_{xrl} & F_{xrr} & F_{yfl} & F_{yfr} & F_{yrl} & F_{yrr}\end{array}\right]^T. \quad (34)$$

Hence, the allocation objective function shown in Eq. (33) can be expressed as the following matrix form:

$$f=x^T W x, \quad (35)$$

where W is the weight matrix which consists of the weight coefficient for each tire A_{ij}, the tire vertical load F_{zij} and the road adhesion coefficient μ.

In order to achieve the optimal dynamic allocation of the tire forces by using the interior-point method, we need to further establish the equality and inequality constraints for system input x, which can be expressed as:

$$\begin{cases} M_z = a(F_{xfl}+F_{xfr})\sin\delta - \dfrac{t_{w1}}{2}(F_{xfl}-F_{xfr})\cos\delta \\ \qquad\qquad -\dfrac{t_{w2}}{2}(F_{xrl}-F_{xrr}) \;\Rightarrow\; c_E(x)=0, \\ (\mu F_{zij})^2-(F_{xij}^2+F_{yij}^2)\geq 0 \;\Rightarrow\; c_I(x)\geq 0\,. \end{cases} \tag{36}$$

In addition to the above equality and inequality constraints, the physical constraints of system input x, i.e. the longitudinal and lateral forces of the four tires, should also be considered and can be represented as $x_{\min}$ and $x_{\max}$, respectively.

4.2. Trust-region interior-point method. Since the dynamic allocation problem considered in this paper involves many variables, complex constraint types and large scales, thus to further accelerate the convergence of the interior-point method and improve the efficiency of the optimization calculation, the interior-point method based on the trust-region is adopted for iterative calculation [52–56]. The KKT conditions for nonlinear programming are rewritten as follows:

$$\begin{cases} \nabla f(x)-A_E^T(x)y-A_I^T(x)z=0, \\ SZ-\eta o=0, \\ c_E(x)=0, \\ c_I(x)-\rho=0, \end{cases} \tag{37}$$

where $A_E(x)$ and $A_I(x)$ are the corresponding Jacobian matrices, $c_E(x)$ and $c_I(x)$ represent the nonlinear equality and inequality constraints in Eq. (36), S and Z are the diagonal matrices whose diagonal terms are given by vectors s and z, and y and z are the Lagrange multipliers of the equality and inequality constraints while o is the column vector whose all elements are one.

On the basis of the given penalty parameter η and the iteration (x,s), the Newton step size p is defined as the iteration step in the optimization process and the solution of the following trust-region subproblem consists of three steps, i.e. calculate the estimation of Lagrange multiplier (y,z), calculate the Newton step size $p=(p_x,p_s)$ and calculate the step size acceptance and judgment.

4.2.1. Calculation of Lagrange multipliers. Firstly, Lagrange multipliers of the equality and inequality constraints (y,z) can be calculated as follows:

$$\begin{bmatrix} y \\ z \end{bmatrix} = \left(\hat{A}\hat{A}^T\right)^{-1}\hat{A}\begin{bmatrix} \nabla f(x) \\ -\eta e \end{bmatrix}, \tag{38}$$

where $\hat{A}$ can be given as follows:

$$\hat{A}=\begin{bmatrix} A_E(x) & 0 \\ A_I(x) & -S \end{bmatrix}. \tag{39}$$

4.2.2. Calculation of Newton step size p. The Newton step size calculation can be transformed into solving the following optimization problems within the constraints of trust region:

$$\min\ \nabla f^T p_x+\frac{1}{2}p_x^T\nabla_{xx}^T L p_x-\eta e^T S^{-1}p_s+\frac{1}{2}p_s^T\Sigma p_s$$
$$s.t.\ \begin{cases} A_E(x)p_x+c_E(x)=r_E \\ A_I(x)p_x-p_s+(c_I(x)-\rho)=r_I \\ \left\|(p_x,S^{-1}p_s)\right\|_2\leq\Delta \\ p_s\geq-\tau\rho \end{cases}, \tag{40}$$

where ∇f and $\nabla_{xx}^T L$ are the gradient and the Hessian matrix, $\Sigma=S^{-1}Z$ is the primal-dual matrix and the scalar $\tau\in(0,1)$ is chosen close to 1, moreover $\Delta>0$ is a trust region radius that is updated at every iteration and r_E and r_I are the residuals in the calculation.

After obtaining the corresponding step size p, the step size can be further redefined to transform the trust region constraint in Eq. (40) into a ball, which is expressed as:

$$\tilde{p}=\begin{bmatrix} p_x \\ \tilde{p}_s \end{bmatrix}=\begin{bmatrix} p_x \\ S^{-1}p_s \end{bmatrix}, \tag{41}$$

then, the constraints on the trust region radius can be written as:

$$\|p_x,\tilde{p}_s\|_2\leq\Delta. \tag{42}$$

The following normal subproblem is constructed with vector $v=(v_x,v_s)$ to obtain vectors r_E and r_I, which can be written as:

$$\min\ \|A_E(x)v_x+c_E(x)\|_2^2+\|A_I(x)v_x-Sv_s+(c_I(x)-s)\|_2^2$$
$$s.t.\ \begin{cases} \|(v_x,v_s)\|_2\leq 0.8\Delta, \\ v_s\geq-(\tau/2)e. \end{cases} \tag{43}$$

By solving the problem in Eq. (43), residuals r_E and r_I can be given by:

$$\begin{cases} r_E=A_E(x)v_x+c_E(x), \\ r_I=A_I(x)v_x-Sv_s+(c_I(x)-\rho). \end{cases} \tag{44}$$

Note that vector v is the particular solution of the linear constraint which is obtained by the gradient projection method.

4.2.3. Calculation of step size acceptance and judgment. In the standard trust-region method, step p is accepted if the following inequality is satisfied:

$$ared(p)\geq\gamma pred(p), \tag{45}$$

where:

$$ared(p) = \varphi_v(x,\rho) - \varphi_v(x+p_x, \rho+p_s), \tag{46}$$

and γ is a number in the range of 0 to 1. The predicted reduction $pred(p)$ is described as:

$$pred(p) = q_v(0) - q_v(p), \tag{47}$$

where:

$$q_v(p) = \nabla f^T p_x + \frac{1}{2} p_x^T \nabla_{xx}^2 L p_x - \eta e^T S^{-1} p_s + \frac{1}{2} p_s^T \Sigma p_s + dm(p), \tag{48}$$

and

$$m(p) = \left\| \begin{bmatrix} A_E(x)p_x + c_E(x) \\ A_I(x)p_x - p_s + c_I(x) - \rho \end{bmatrix} \right\|_2, \tag{49}$$

Consequentially, the exact merit function appears in Eq. (46) and is defined as:

$$\varphi_v(x,\rho) = J - \eta \sum_{i=1}^{4} \log(s_i) + d\,\|c_E(x)\| + d\,\|c_I(x) - \rho\|, \tag{50}$$

where d is the penalty parameter, which must be large enough to satisfy the inequality as follows:

$$pred(p) \geq pd(m(0) - m(p)). \tag{51}$$

5. Simulation results and analyses

In this section, the effectiveness of the proposed DYC system, which considers the coupling relationship of the tire forces in the STI form, uses the NFTSM control algorithm to calculate the optimal direct yaw moment and adopts the trust-region interior-point method to achieve the tire forces allocation of four wheels, for a four-wheel independent drive autonomous electric vehicle, is verified by simulation results. To accurately reflect the nonlinear dynamic characteristics of electric vehicles, which are consistent with the starting conditions of the DYC system, the CarSim vehicle model is further adopted.

Considering the driving conditions corresponding to the DYC system, two simulation cases in which the road adhesion coefficients are set to 0.6 and 0.3, respectively, are provided in this work. By conducting efficient simulation comparisons, the parameters of the NFTSM control system are determined as follows: $c_1 = 0.5$, $\alpha_1 = 1$, $\beta_1 = 1$, $p_1 = 5$, $q_1 = 3$, $k_1 = 0.2$, $r_1 = 1$, $m_1 = 9$, $n_1 = 7$, $g_1 = 5$, $h_1 = 3$. In the co-simulation procedure, the vehicle is assumed to track two different paths at the desired speed of 70 km/h ($\mu = 0.6$) and 40 km/h ($\mu = 0.3$), respectively. The vehicle parameters adopted in the CarSim-Simulink co-simulation are provided in Table 2.

Table 2
Vehicle simulation parameters

Parameters	Value
Total mass of vehicle, m (kg)	1110
Moment of inertia, I_z (kg·m^2)	1343.1
Longitudinal distance of cog to front axle, a (m)	1.04
Longitudinal distance of cog to front axle, b (m)	1.56
Front wheel tread, t_{w1} (m)	1.65
Rear wheel tread, t_{w2} (m)	1.65
Front tire cornering stiffness, k_f (N/rad)	–4000
Rear tire cornering stiffness, k_r (N/rad)	–4000
Moment of inertia of the wheel, J (kg·m^2)	32
Wheel radius, R (m)	0.3
Height of vehicle center, h_g (m)	0.36

5.1. Simulation results of sine steering angle input. In the first simulation, a sine steering angle input with an amplitude of 90° is employed and the simulation results comparison of the vehicle slip angle, yaw rate and the obtained direct yaw moment between the NFTSM and the SMC are shown in Fig. 4. As can be seen from Fig. 4(a) and Fig. 4(b), the peak values of the vehicle slip angle and the vehicle yaw rate controlled by the NFTSM decrease significantly as compared with that controlled by the SMC, among which the absolute value of the vehicle slip angle peak value is reduced from 0.01 rad to 0.007 rad and the absolute value of the vehicle yaw rate peak value is reduced from 0.18 rad to 0.14 rad, which demonstrates the effectiveness of the proposed DYC approach for the four-wheel independent drive electric vehicle steering with high speed and better tracking effect for the reference model. Figure 4(c) shows the difference of the direct yaw moment between the NFTSM and the SMC. It is obvious that the direct yaw moment calculated by the two methods is different, which illustrates that the proposed DYC approach in this work can effectively calculate an optimal direct yaw moment by considering the tire forces constraints and coupling relationship under high speed steering conditions.

To achieve the direct yaw moment and guarantee path tracking accuracy, optimal allocation of the tire forces is conducted. Figure 5 shows the allocation results of the tire longitudinal forces of the four wheels. It can be seen that different tire forces of the four wheels have been optimally allocated to achieve the direct yaw moment. In addition, for analyzing the influence of no-load and full load on the tire force distribution results, it can be seen that the force distribution results of the right front wheel F_{xfr} and the right rear wheel F_{xrr} are larger than those of the left front wheel F_{xfl} and the left rear wheel F_{xrl}. Thus, it can be concluded that, due to the load transfer effect, the vertical load of the two right wheels is greater than that of the two left wheels and that the longitudinal force of the tire distribution increases when the wheel radius decreases.

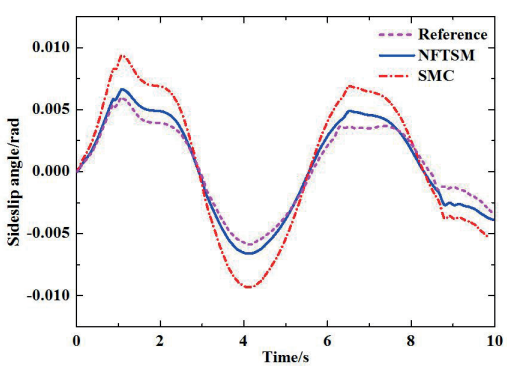

(a) Comparison of vehicle slip angle

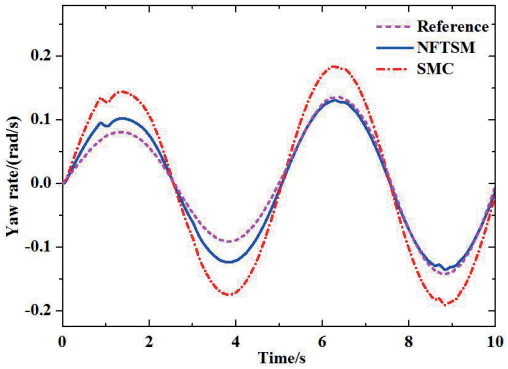

(b) Comparison of vehicle yaw rate

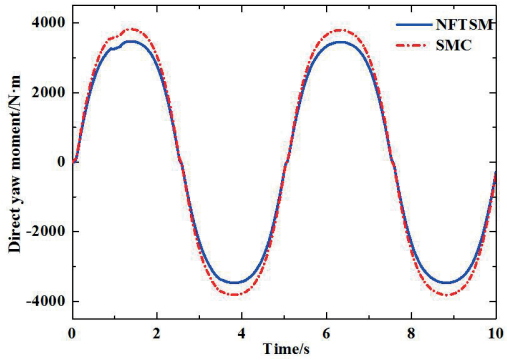

(c) Comparison of the calculated direct yaw moment

Fig. 4. Simulation results comparison between NFTSM and SMC ($\mu = 0.6$)

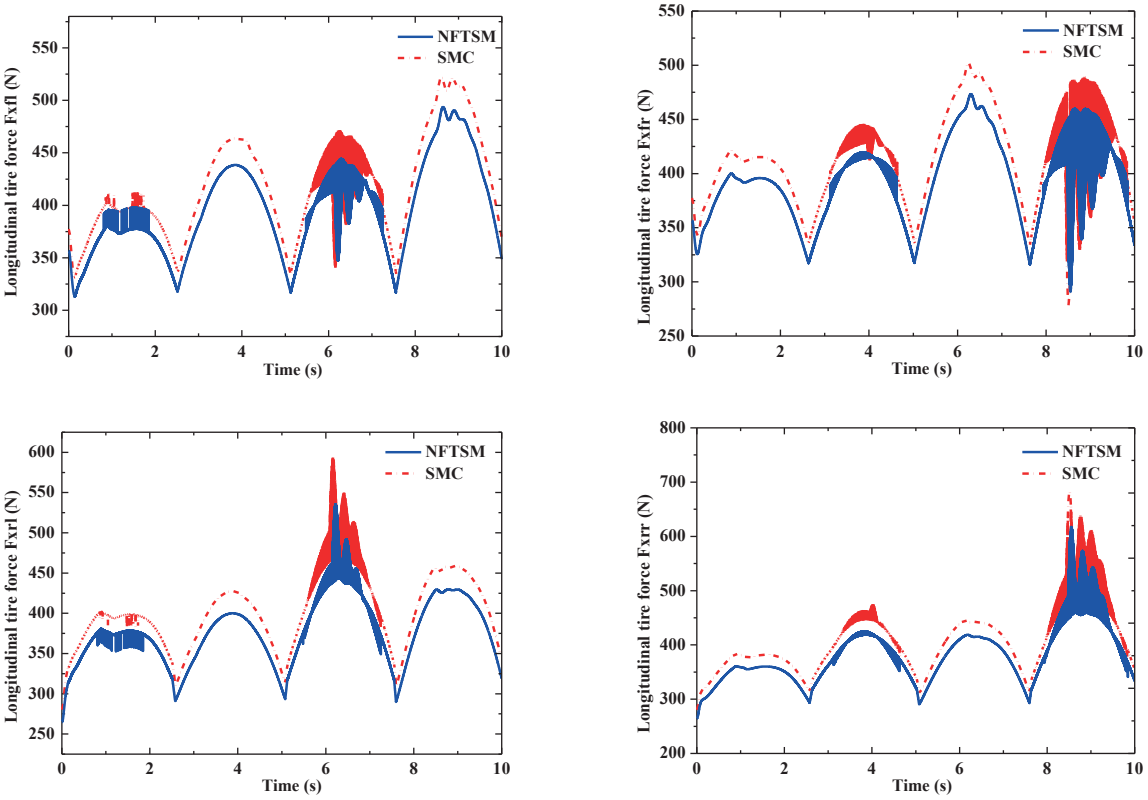

Fig. 5. Tire forces allocation based on the trust-region interior-point method ($\mu = 0.6$)

5.2. Simulation results of double lane change. Similarly, the double lane change input with the lateral offset of 3.5 m is adopted and the simulation results comparison of the vehicle slip angle, the vehicle yaw rate and the obtained direct yaw moment between the NFTSM and the SMC for the second case are shown in Fig. 6. As can be seen from Fig. 6(a) and Fig. 6(b), the peak values of the vehicle slip angle and the vehicle yaw rate controlled by the NFTSM also decrease significantly as compared with that controlled by the conventional SMC, among which the absolute value of the vehicle slip angle peak value is reduced from 0.008 rad to 0.005 rad and the absolute value of the vehicle yaw rate peak value is reduced from 0.3 rad to 0.2 rad.

The difference of the direct yaw moment between the NFTSM and the SMC is shown in Fig. 6(c). Same conclusion can be obtained as in the first case, i.e. the direct yaw moment calculated by the two methods is different, which shows that the optimal direct yaw moment can be effectively calculated by the NFTSM.

The allocation results of the tire longitudinal forces of the four wheels in the second case are shown in Fig. 7. Compared with the allocation results of the tire forces shown in Fig. 5, it can be seen that the tire forces of the four wheels in the second case are obviously smaller than that in the first case, which is due to the smaller road adhesion coefficients. In this case, the tire-road friction force reduces. This phenomenon shows that the optimal allocation of the tire forces based on the trust-region interior-point method can effectively reflect the coupling relationship between the tire longitudinal force and tire lateral force as well as the tire force constraints on a slippery road, thus the resulting tire forces can then be achieved through the actuators of the four-wheel independent drive autonomous electric vehicle in practical applications.

Note that although an excessive switching rate can be noticed for the tire forces, the variation characteristics of the tire forces are actually different from that of the driving or braking torques acting on the four wheels. By checking the results of the torques acting on the four wheels, it can be found that the switching rate of the motor torque is available for standard motors. However, considering the importance of presented results and the paper limitations, the relevant figures are not presented.

In the simulation process, we have also found that the calculation time of the dynamic allocation problem through the trust-region interior-point method is about 35 ms, while the calculation time of the traditional interior-point method is about 120 ms, which shows that the real-time performance of the trust-region interior-point method adopted in this work is better than that of the contrast method.

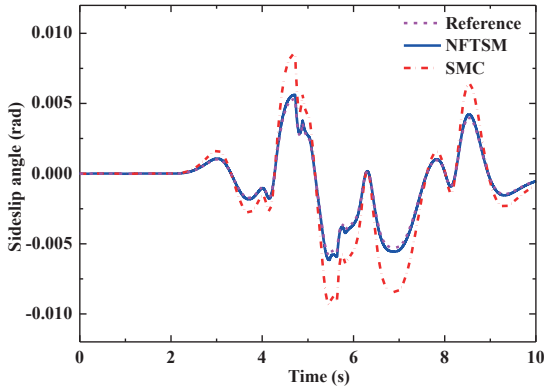

(a) Comparison of vehicle slip angle

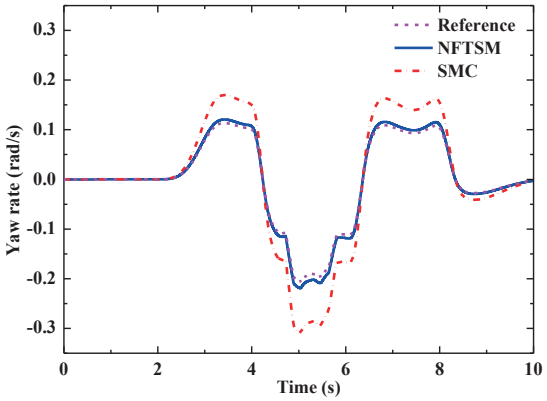

(b) Comparison of vehicle yaw rate

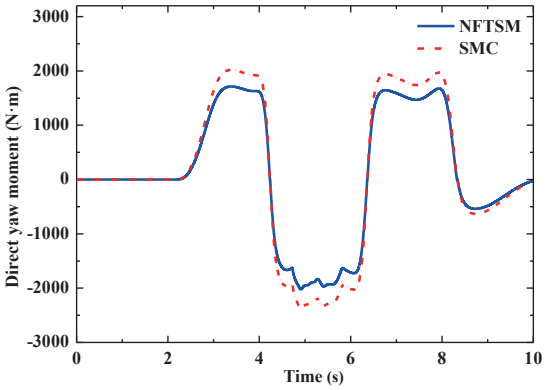

(c) Comparison of the calculated direct yaw moment

Fig. 6. Simulation results comparison between NFTSM and SMC ($\mu = 0.3$)

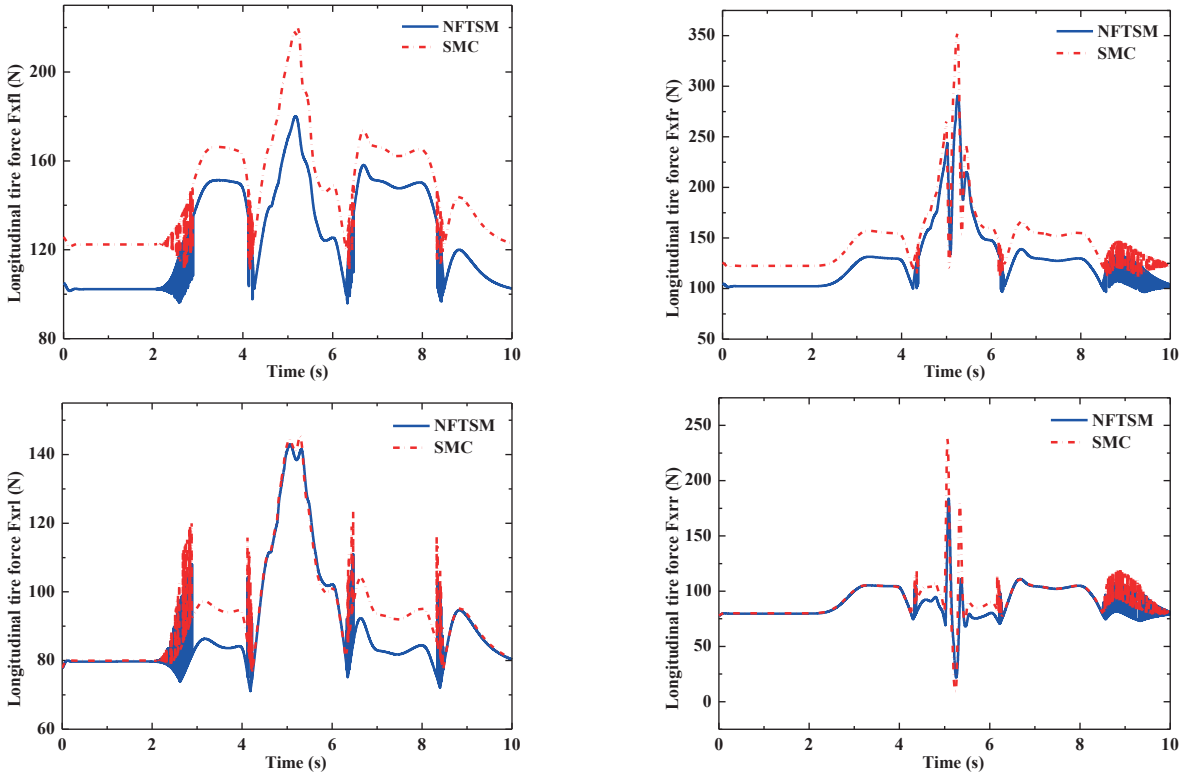

Fig. 7. Tire forces allocation based on the trust-region interior-point method ($\mu = 0.3$)

6. Conclusions

This work proposed a novel three-stage DYC system design procedure, which considers the coupling relationship of the tire forces in the STI form, uses the NFTSM control algorithm to calculate the optimal direct yaw moment and adopts the trust-region interior-point method to achieve the tire forces allocation of four wheels, for the four-wheel independent drive autonomous electric vehicles. Based on the experimental data, the STI tire model with fitted parameters can accurately describe the tire nonlinear mechanical properties and the coupling relationship between the tire longitudinal force and the tire lateral force. On this basis, a 7-DOF dynamics model of the electric vehicle is established and the optimal direct yaw moment calculation problem is solved through the NFTSM control algorithm. To achieve the derived direct yaw moment, the optimal allocation of the tire forces is further conducted using the trust-region interior-point method. CarSim-Simulink co-simulation results are finally provided to verify the effectiveness of the proposed DYC strategy. In the simulation procedure, two simulation cases are designed and all the co-simulation results show that the peak values of the vehicle slip angle and the vehicle yaw rate controlled by the NFTSM decrease significantly as compared with that controlled by the conventional SMC, which demonstrates that the vehicle motion stability when tracking curve paths under critical maneuvers is improved by using the NFTSM method. Therefore, this work is essential for moving forward the scientific and industrial knowledge of the DYC system design of the four-wheel independent drive autonomous electric vehicles.

Acknowledgments. This work was supported by the National Natural Science Foundation of China (Grant No. 52072161 and 51875255), the China Postdoctoral Science Foundation (Grant No. 2019T120398), the State Key Laboratory of Automotive Safety and Energy (Grant No. KF2016) and the Young Elite Scientists Sponsorship Program by CAST (Grant No. 2018QNRC001).

References

[1] H. Wang, K. Xu, Y. Cai, and L. Chen, "Trajectory planning for lane changing of intelligent vehicles under multiple operating conditions", *J. Jiangsu Univ. Nat. Sci.* 40(3), 255–260 (2019).

[2] Y. Li, B. Zhang, and X. Xu, "Robust control for permanent magnet in-wheel motor in electric vehicles using adaptive fuzzy neural network with inverse system decoupling", *Trans. Can. Soc. Mech. Eng.* 42(3), 286–297 (2018).

[3] Y. Li, H. Deng, X. Xu, and W. Wang, "Modelling and testing of in-wheel motor drive intelligent electric vehicles based on co-simulation with Carsim/Simulink", *IET. Intell. Transp. Syst.* 13(1), 115–123 (2019).

[4] D. Zhang, G. Liu, H. Zhou, and W. Zhao, "Adaptive sliding mode fault-tolerant coordination control for four-wheel independently driven electric vehicles", *IEEE. Trans. Ind. Electron.* 65(11), 9090–9100 (2018).

[5] T. Chen, X. Xu, L. Chen, H. Jiang, Y. Cai, and Y. Li, "Estimation of longitudinal force, lateral vehicle speed and yaw rate for four-wheel independent driven electric vehicles", *Mech. Syst. Signal. Process.* 101, 377–388 (2018).

[6] T. Chen, X. Xu, Y. Cai, H. Jiang, and X. Sun, "Reliable sideslip angle estimation of four-wheel independent drive electric vehicle by information iteration and fusion", *Math. Probl. Eng.* 2018, 9075372 (2018).

[7] H. Zhang, J. Liang, H. Jiang, Y. Cai, and X. Xu, "Stability research of distributed drive electric vehicle by adaptive direct yaw moment control", *IEEE Access.* 7, 106225–106237 (2019).

[8] L.D. Novellis, A. Sorniotti, P. Gruber, J. Orus, J.R. Fortun, J. Theunissen and J. D. Smet, "Direct yaw moment control actuated through electric drivetrains and friction brakes: Theoretical design and experimental assessment", *Mechatronics.* 26, 1–15 (2015).

[9] Y. Chen, J. Hedrick, and K. Guo, "A novel direct yaw moment controller for in-wheel motor electric vehicles", *Veh. Syst. Dyn.* 51(6), 925–942 (2013).

[10] A. Goodarzi, F. Diba, and E. Esmailzadeh, "Innovative active vehicle safety using integrated stabilizer pendulum and direct yaw moment control", *J. Dyn. Syst-Trans. ASME.* 136(5), DS-12-1335 (2014).

[11] S. Ding and J. Sun, "Direct yaw-moment control for 4WID electric vehicle via finite-time control technique", *Nonlinear Dyn.* 88(1), 239–254 (2017).

[12] S. Ding, L. Liu, and W. Zheng, "Sliding mode direct yaw-moment control design for in-wheel electric vehicles", *IEEE. Trans. Ind. Electron.* 64(8), 6752–6762 (2017).

[13] W. Huang, P. Wong, K. Wong, C. Vong, and J. Zhao, "Adaptive neural control of vehicle yaw stability with active front steering using an improved random projection neural network", *Veh. Syst. Dyn.* 59(3), 396–414 (2021), doi: 10.1080/00423114.2019.1690152.

[14] J. Wagner and J. Keane, "A strategy to verify chassis controller software-dynamics, hardware, and automation", *IEEE Trans. Syst. Man Cybern. Part A-Syst. Hum.* 27(4), 480–493 (1997).

[15] M. Reiter and J. Wagner, "Automated automotive tire inflation system–effect of tire pressure on vehicle handling", *IFAC Proceedings* 47(3), 638–643 (2010).

[16] Y. Shi, Q. Liu, and F. Yu, "Design of an adaptive FO-PID controller for an in-wheel-motor driven electric vehicle", *SAE Int. J. Commer. Veh.* 10, 265–274 (2017).

[17] H. Guo, F. Liu, F. Xu, H. Chen, D. Cao, and Y. Ji, "Nonlinear model predictive lateral stability control of active chassis for intelligent vehicles and its FPGA implementation", *IEEE Trans. Syst. Man Cybern. Part A-Syst. Hum.* 49(1), 2–13 (2017).

[18] Q. Meng, T. Zhao, C. Qian, Z. Sun, and P. Ge, "Integrated stability control of AFS and DYC for electric vehicle based on non-smooth control", *Int. J. Syst. Sci.* 49(7), 1518–1528 (2018).

[19] J. Song, "Development and comparison of integrated dynamics control systems with fuzzy logic control and sliding mode control", *J. Mech. Sci. Technol.* 27(6), 1853–1861 (2013).

[20] J. Wang and R. He, "Hydraulic anti-lock braking control strategy of a vehicle based on a modified optimal sliding mode control method", *Proc. Inst. Mech. Eng. Part D-J. Aut.* 233(12), 3185–3198 (2019).

[21] X. Sun, Y. Cai, C. Yuan, S. Wang, and L. Chen, "Fuzzy sliding mode control for the vehicle height and leveling adjustment system of an electronic air suspension", *Chin. J. Mech. Eng.* 31(25), (2018), doi. 10.1186/s10033-018-0223-8.

[22] S. Chen, J. Wang, M. Yao, and Y. Kim, "Improved optimal sliding mode control for a non-linear vehicle active suspension system", *J. Sound. Vib.* 395, 1–25 (2017).

[23] Z. Yang, D. Zhang, X. Sun, W. Sun, and L. Chen, "Nonsingular Fast Terminal Sliding Mode Control for a Bearingless Induction Motor", *IEEE Access.* 5, 16656–16664 (2017).

[24] E. Mousavinejad, Q. Han, F. Yang, Y. Zhu, and L. Vlacic, "Integrated control of ground vehicles dynamics via advanced terminal sliding mode control", *Veh. Syst. Dyn.* 55(2), 268–294 (2017).

[25] A. Asiabar and R. Kazemi, "A direct yaw moment controller for a four in-wheel motor drive electric vehicle using adaptive sliding mode control", *Proc. Inst. Mech. Eng. Part K-J. Multi-Body Dyn.* 233(3), 549–567 (2019).

[26] J. Zhang and J. Li, "Integrated vehicle chassis control for active front steering and direct yaw moment control based on hierarchical structure", *Trans. Inst. Meas. Control.* 41(9), 2428–2440 (2019).

[27] S. Yue and Y. Fan, "Hierarchical direct yaw-moment control system design for in-wheel motor driven electric vehicle", *Int. J. Automot. Technol.* 19(4), 695–703 (2018).

[28] X. Chen, J. Yang, D. Zhang, and J. Liang, "Complete large margin linear discriminant analysis using mathematical programming approach", *Pattern Recogn.* 46(6), 1579–1594 (2013).

[29] R.H. Byrd, M.E. Hribar, and J. Nocedal, "An interior point algorithm for large-scale nonlinear programming", *SIAM J. Optim.* 9(4), 877–900 (1999).

[30] R.H. Byrd, J.C. Gilbert, and J. Nocedal, "A trust region method based on interior point techniques for nonlinear programming", *Math. Progr*. 89(1), 149–185 (2000).

[31] K. Pan and Y. Lu, "Analysis on vehicle dynamic simulating sti tire model used in driving simulator", *Auto Eng.* 2, 28–30 (2009).

[32] Q. Xia, L. Chen, X. Xu, Y. Cai, H. Jiang, T. Chen, and G. Pan, "Running states estimation of autonomous four-wheel independent drive electric vehicle by virtual longitudinal force sensors", *Math. Probl. Eng.* 2019, 8302943 (2019), doi: 10.1155/2019/8302943.

[33] J. Tian, J. Tong, and S. Luo, "Differential steering control of four-wheel independent-drive electric vehicles", *Energies* 11(11), 2892 (2018).

[34] T. Chen, X. Xu, Y. Li, W. Wang, and L. Chen, "Speed-dependent coordinated control of differential and assisted steering for in-wheel motor driven electric vehicles", *Proc. Inst. Mech. Eng. Part D-J. Automob. Eng.* 232(9), 1206–1220 (2018).

[35] L. Chen, T. Chen, X. Xu, Y. Cai, H. Jiang, and X. Sun, "Multi-objective coordination control strategy of distributed drive electric vehicle by orientated tire force distribution method", *IEEE Access.* 6, 69559–69574 (2018).

[36] P. Herman and W.Adamski, "Non-adaptive velocity tracking controller for a class of vehicles", *Bull. Pol. Acad. Sci. Tech. Sci.* 65(4) 459–468 (2017).

[37] Y. Li, H. Wu, X. Xu, Y. Cai, and X. Sun, "Analysis on electromechanical coupling vibration characteristics of in-wheel motor in electric vehicles considering air gap eccentricity", *Bull. Pol. Acad. Sci. Tech. Sci.* 67(5), 851–862 (2019).

[38] X. Zhang, H. He, J. Nie, and L. Chen, "Performance analysis of semi-active suspension with skyhook-inertance control", *J. Jiangsu Univ. Nat. Sci.* 39(5), 497–502 (2018).

[39] Y.Li, B.Zhang, and X.Xu, "Decoupling control for permanent magnet in-wheel motor using internal model control based on back-propagation neural network inverse system", *Bull. Pol. Acad. Sci. Tech. Sci.* 66(6), 961–972 (2018).

[40] S. Jiang, P. Wong, R. Guan, Y. Liang, and J. Li, "An efficient fault diagnostic method for three-phase induction motors based on incremental broad learning and non-negative matrix factorization", *IEEE Access* 9, 17780–17790 (2019).

[41] H. Ye, G. Li, S. Ding, and H. Jiang, "Direct yaw moment control of electric vehicle based on non-smooth control technique", *J. Jiangsu Univ. Nat. Sci.* 39(6), 640–646 (2018).

[42] H. Qiu, Z. Dong, and Z. Lei, "Simulation and experiment of integration control of ARS and DYC for electrical vehicle with four wheel independent drive", *J. Jiangsu Univ. Nat. Sci.* 37(3), 268–276 (2016).

[43] S. Ding, L. Liu, and J. H. Park, "A novel adaptive nonsingular terminal sliding mode controller design and its application to active front steering system", *Int. J. Robust Nonlinear Control* 29(12), 4250–4269 (2019).

[44] S. Ding and W. Zheng, "Nonsingular terminal sliding mode control of nonlinear second-order systems with input saturation", *Int. J. Robust Nonlinear Control* 26(9) 1857–1872 (2016).

[45] H. Jiang, F. Cao, and W. Zhu, "Control method of intelligent vehicles cluster motion based on SMC", *J. Jiangsu Univ. Nat. Sci.* 39(4), 385–39 (2018).

[46] B. Xu, G. Shi, W. Ji, F. Liu, and S. Ding, H. Zhu, "Design of an adaptive nonsingular terminal sliding model control method for a bearingless permanent magnet synchronous motor", *Trans. Inst. Meas. Control* 39(12), 1821–1828 (2017).

[47] X. Yu, J. Yin, and S. Khoo, "Generalized Lyapunov criteria on finite-time stability of stochastic nonlinear systems", *Automatica* 107,183–189 (2019).

[48] Y. Ma, Z. Zhang, Z. Niu, and N. Ding, "Design and verification of integrated control strategy for tractor-semitrailer AFS/DYC", *J. Jiangsu Univ. Nat. Sci.* 39(5), 530–536 (2018).

[49] J. Wang, X. Yu, Z. Hui, and X. Hu, "Influence of running speed and lateral distance on vehicle transient aerodynamic characteristics during curve crossing", *J. Jiangsu Univ. Nat. Sci.* 38(3), 249–253 (2017).

[50] C. Huang, L. Chen, C. Yun, H. Jiang, and Y. Chen, "Integrated Control of Lateral and Vertical Vehicle Dynamics Based on Multi-agent System", *Chin. J. Mech. Eng.* 27(2), 304–318 (2014).

[51] W. Liu, R. Wang, C. Xie, and Q. Ye, "Investigation on adaptive preview distance path tracking control with directional error compensation", *Proc. Inst. Mech. Eng. Part I-J. Syst. Control Eng.* 234(4), 484–500 (2019), doi: 10.1177/0959651819865789.

[52] T. Coleman and Y. Li, "A trust region and affine scaling interior point method for nonconvex minimization with linear inequality constraints", *Math. Progr.* 88(1), 1–31 (2000).

[53] F. Leibfritz and E. Mostafa, "An interior point constrained trust region method for a special class of nonlinear semidefinite programming problems", *SIAM J. Optim.* 12(4), 1048–1074 (2002).

[54] M. Rojas and T. Steihaug, "An interior-point trust-region-based method for large-scale non-negative regularization", *Inverse Probl.* 18(5), 1291–1307 (2002).

[55] J. Bonnans and C. Pola, "A trust region interior point algorithm for linearly constrained optimization", *SIAM J. Optim.* 7(3), 717–731 (1997).

[56] J. Erway and P. Gill, "A subspace minimization method for the trust-region step", *SIAM J. Optim.* 20(3), 1439–1461 (2010).